Contents lists available at ScienceDirect

International Journal of Mechanical Sciences

journal homepage: www.elsevier.com/locate/ijmecsci

Buckling of stretched disks—With comparisons and extensions to auxetics

Saeideh Faghfouri, Franz G. Rammerstorfer *

Vienna University of Technology (TU Wien), Institute of Lightweight Design and Structural Biomechanics, Vienna, Austria

ARTICLE INFO

ABSTRACT

In this paper, we investigate the instability behavior of thin elastic circular disks subjected to two concentrated edge loads arranged along a diameter. Despite the determination of critical load intensities for disks, made of conventional, linear elastic material, under some specific boundary conditions has been published in the past, we show some new and quite interesting findings. Particularly new are the investigations of tensile buckling of completely free disks as well as the post-buckling behavior of such disks under tension and compression, respectively. Comparisons with already existing results are presented, too. As far as the buckling load is concerned, all results are expressed in terms of a non-dimensional buckling factor.

It is well known that the use of auxetic materials provides some potential for improving the behavior of lightweight structures. This fact has motivated us to consider, in which way the variation of the Poisson's ratio ν influences the stability behavior of the disks both under compression and under tension not just for the so far not investigated completely free stretched disks but also for the already published configurations. The Poisson's ratio is varied in the full thermodynamically admissible range $[-1.0, 0.5]$ and some quite peculiar results are found and explained, especially for disks made of auxetic materials, i.e. for $\nu < 0$. Although the stress fields are independent of the value of ν, the dependency of the critical load intensities is not simply proportional to the dependency of the plate's bending stiffness on ν, and the buckling modes show significant changes when ν is varied.

The buckling factors for disks under tensile loading are by an order of magnitude larger than those for the compressed disks. Of course, also the buckling modes differ completely between compression and tension. Furthermore, the post-buckling behavior is qualitatively and quantitatively significantly different, too.

The considerations and the achieved results are interesting for scientists working in the field of structural stability and for engineers in lightweight design of structures. Furthermore, there are applications in the design of sensors and actors as well as of flexible electronics. Since similar thin membrane structures appear in biological tissues, the paper might be interesting also for biologists.

1. Introduction

Buckling of circular disks might seem like an old-fashioned and long-dated subject. Indeed, there exist numerous classical papers treating buckling of circular disks made of homogeneous, isotropic material under different loading and boundary conditions, see e.g. [1,2] and the papers cited therein. Rotationally symmetrical buckling of disks under uniform radial loading has been used as a typical class-room example for the application of the Ritz method in structural stability, e.g. in [3]. The influence of residual stresses on the instability of circular plates has been treated in [4]. The stability of circular disks made of composite and other complex materials has been treated in more recent papers; see, for instance, [5] and papers cited therein.

More specifically, buckling of circular disks subjected to arbitrarily distributed radial loadings has been treated decades ago in [6], and

investigations of instabilities of disks under two concentrated forces acting along a diameter can be found in [7] and in [8].

Typically, buckling is related to compressive loading. However, under certain conditions also tensile loading of thin-walled structures may lead to buckling, see, e.g., [9–19], and [20] as well as papers cited therein. As far as we know, it was Durban who in [6] first pointed out the possibility of buckling of circular disks under radial tensile forces. In [21,22] the stability of tension loaded mechanical systems consisting of thin beams whose unloaded ends are guided in rigid rails, is considered.

It might be amazing that, despite the fact that buckling of disks has been considered for a long time, we take up this topic again. Our motivation for this is diverse: (i) One of the most interesting configurations for investigating instabilities of circular disks under
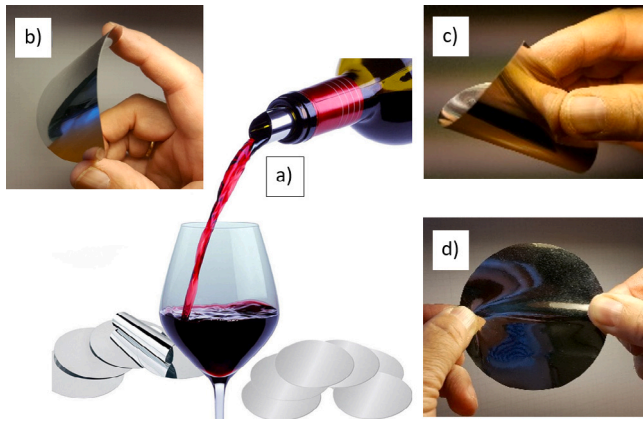

Fig. 1. Bottle pourer; (a) undeformed pourer disks and pourer in use; (b) buckling under compression; (c) curling; (d) buckling by stretching.

Table 1
Definition of the considered CASEs.

Definitions	Boundary and loading condition	
Completely free		Simply supported
Tension CASE A Compress. CASE B		Tension CASE C Compress. CASE D

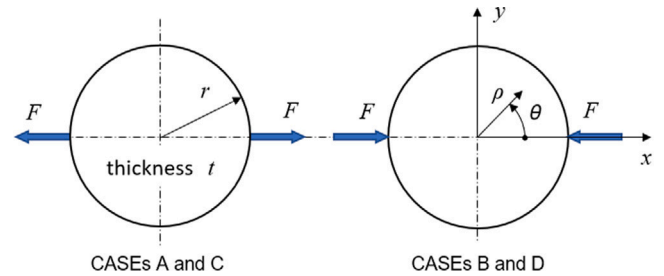**Fig. 2.** Configurations under consideration; CASEs A and B: completely free; CASEs C and D: simply supported along the whole boundary edge.

diametrical point forces, namely the completely free stretched disk, was not yet treated in the open literature. (ii) We have been expecting interesting effects when considering disks made of auxetic materials. However, we could not find related published results. (iii) Based on our experimental observations (see, e.g., Fig. 1), we intended to investigate the post-buckling behavior of such disks, expecting some new results.

With respect to using auxetics in lightweight design (see item (ii)) we refer, for instant, to [23,24]. Methods and models for the design and characterization of auxetic materials can be found, e.g., in [25,26] as well as in papers cited therein.

Regarding items (i) and (iii), we invite the reader to mess around with a wine bottle pourer in the form of a thin metallic circular disk, see Fig. 1(a). If one uses such a bottle pourer for the purpose which it is made for, the disk is typically brought to buckle by compressing it between the index finger and thumb, see Fig. 1(b), followed by curling up it (as a post-bucking action), see Fig. 1(c), so that it can be put into the bottleneck as shown in Fig. 1(a). This is a quite easy task. However, it is by far not an easy task to make the pourer disk buckle by stretching it along a diameter, see Fig. 1(d).

Generally, we have been motivated by the fact, that results should be interesting for people working in structural mechanics and in materials sciences, as well as in biomechanics. Potential applications are in lightweight structural design, in the design of sensors and actors, and of membranes in process plats etc. The results are also useful for studying membranes in biological structures, as they are, for instant, considered in [27,28].

For determining the buckling load for the situation as shown in Fig. 1(b), the solution, as presented in [7], could be used. However, to the knowledge of the authors, the most interesting situation, as described in Fig. 1(d), has not been fully elaborated in the literature yet.

2. Models and methods

In [7], the critical intensity for buckling of the fully free disk under diametrical compressive forces is analyzed by iteratively solving the eigenvalue problem resulting from the leading differential equations after developing the displacement function in Fourier series. In [6] both the distribution of the in-plane edge loading and the buckling modes are developed in Fourier series in order to allow the determination of critical intensities of arbitrarily distributed loads, including situations as depicted in Fig. 2, under the assumption of simple support conditions along the whole circumference of the circle. The Ritz approach, which is described in [8] could, in principle, also be applied for estimating critical tensile forces for clamped, simply supported, and free boundaries. However, in [8] only the case of a simply supported boundary has been elaborated in full detail as far as the buckling load is concerned.

In the present paper we applied the finite element method. Thereby, not only the most interesting and not yet solved problem of the completely free disk under tensile loading – denoted as CASE A in the following – has been considered, but also the already known solutions for critical loads for tension and compression of disks, which are simply supported along the whole boundary (CASEs D and C), as well as for compression of the completely free disk (CASE B) are discussed for comparison reasons.

Linear elastic, isotropic material with Young's modulus E and Poisson's ratio ν was assumed. In order to demonstrate in which way the Poisson's ratio ν influences the critical load intensity and the buckling mode of the CASEs defined in Table 1, the value of ν was varied within the thermodynamically admissible range, i.e. $-1.0 < \nu < 0.5$. Because in all of the above mentioned existing papers, stability of circular disks under concentrated loads has been treated for $\nu \geq 0$, we were specifically interested in new results describing the behavior of disks made of materials with $\nu < 0$, i.e., disks made of auxetic materials.

3. Procedures for eigenvalue buckling analysis and post-buckling simulation

We employed the finite element method in our analyses with carefully designed models. This means, we used a very fine mesh in order to compute the quite inhomogeneous stress fields accurately as well as to sufficiently resolve the buckling modes and post-buckling deformations. By this way we were able to perform meaningful comparisons with the already published results in terms of critical load intensities for CASEs B, C, and D, which we extended to disks made of auxetic materials and to the not yet considered CASE A. Furthermore, we performed cross checks between results obtained by using our non-commercial research FE-code CARINA (*C*omputer *A*ided *R*esearch *In* *N*onlinear *A*nalysis; see [29]) and the commercial FE-package ABAQUS [30] for ensuring high quality of the results.

3.1. Buckling analysis

Eigenvalue buckling analysis, based on Euler's buckling criterion, was used to determine the critical load, i.e., bifurcation or buckling load. In this way, we looked for the load intensities for which the tangent stiffness matrix $\mathbf{K}$ becomes singular, so that in the critical state (denoted by *) the incremental equilibrium condition, $\mathbf{K}^* \delta \mathbf{u} = \delta \boldsymbol{F}_{ext} = \mathbf{0}$, has nontrivial solutions $\delta \mathbf{u} \neq \mathbf{0}$. We assumed proportional loading, i.e., $^m \boldsymbol{F}_{ext} = {}^m \lambda \, \boldsymbol{F}_{ref}$, where $^m \boldsymbol{F}_{ext}$ is the external nodal force vector at state m, $\boldsymbol{F}_{ref}$ is the chosen reference load vector, and $^m \lambda$ is the load multiplier at state m.

When using CARINA in Total Lagrangian (TL) formulation, the linearized eigenvalue problem resulting from Euler's buckling criterion reads for negligibly small pre-buckling deformations:

$$[\mathbf{K}_0 + \eta(\mathbf{K}_u^{lin}(\lambda = 1) + \mathbf{K}_g^{lin}(\lambda = 1))]\,\boldsymbol{\phi} = \mathbf{0}\,. \tag{1}$$

With the eigenvalue η_i, the buckling load of order i is given by $F_i^* = \eta_i F_{ref}$, and the eigenvector $\boldsymbol{\phi}_i$ represents, in conjunction with the elements' shape functions, the corresponding buckling mode.

In Eq. (1) $\mathbf{K}_0$ is the stiffness matrix in the unloaded situation; $\mathbf{K}_u^{lin}(\lambda = 1)$ and $\mathbf{K}_g^{lin}(\lambda = 1)$ are the linearized form of the initial displacement matrix and of the initial stress matrix, respectively, at load level $\lambda = 1$.

In order to avoid that for the tensile loaded disks, i.e. CASEs A and C, negative eigenvalues η are computed, F_{ref} should be chosen to be close to the expected F_1^*. The exclusion of negative eigenvalues is necessary because they would correspond to critical load intensities under compression instead of the wanted critical load intensities for tension.

In the commercial FE-package ABAQUS, the tangent stiffness matrix $\mathbf{K}$ is determined according to an Updated Lagrangian formulation (UL), and the eigenvalue problem reads

$$[\mathbf{K}_P + \kappa\mathbf{K}_\Delta]\,\boldsymbol{\phi} = \mathbf{0}\,. \tag{2}$$

$\mathbf{K}_P$ is the tangent stiffness matrix corresponding to a current base state, which includes the effects of a prescribed preload P, and $\mathbf{K}_\Delta$ is the differential stiffness matrix due to a small incremental loading Q. The eigenvalues κ_i are used for determining the critical loads by

$$F_i^* = P + \kappa_i Q\,. \tag{3}$$

Since we assumed that a linear buckling analysis suffices, we took the unloaded state, $P = 0$, as the base state and defined $Q = F_{ref}$. ABAQUS enables the exclusion of negative eigenvalues by using a Lanczos eigenvalue solver [31], which allows the definition of the search interval, for calculating the eigenvalues from Eq. (3). The critical load vector of ith order is given by $F_i^* = \kappa_i F_{ref}$, and the eigenvector $\boldsymbol{\phi}_i$ determines the corresponding buckling mode.

According to the loading states sketched in Fig. 2, all components of the vector F_{ref} are zero, except those, which correspond to the two external loads, denoted as F in Fig. 2. The most relevant buckling load is F_1^*. Therefore, if in the following F^* is used without a subscript, F_1^* is meant.

3.2. Post-buckling analysis

Incremental–iterative analyses in an Updated Lagrangian (UL) framework, using full Newton–Raphson iterations were performed for simulating the post-buckling behavior. In order to ensure that the equilibrium path after bifurcation does not follow the unstable trivial path, we used models, which were made slightly imperfect. Geometric imperfections were brought into the disks by adding small values to the coordinates of the nodal points in a way that the imperfection is affine to the first buckling mode:

$$X_{imp} = X + \mu\,t\,\boldsymbol{\phi}_{trans}\,. \tag{4}$$

There, X and X_{imp} are the vectors of the perfect and imperfect, respectively, nodal point coordinates, and $\boldsymbol{\phi}_{trans}$ contains the translational components of the normalized eigenvector $\boldsymbol{\phi}_1$. With the imperfection parameter μ and a characteristic length h of the considered structure, μh gives the amplitude of the imperfection. We used the plate thickness t as characteristic length and gave μ values in the range of a few percent.

4. Results and discussions

4.1. Stresses responsible for buckling

For compressed disks (CASEs B and D) it is quite obvious that buckling is caused by compressive stresses in x-direction (coordinate system according to Fig. 2). It is not that obvious, why and by which compressive stresses buckling happens under tensile loading (CASEs A and C). This becomes clearer by consideration of the distribution of the normal stresses in x- and y-direction.

Closed-form solutions for the distributions of the stresses for the CASEs A and C have been derived in [8] in polar coordinates (ρ, θ), according to Fig. 2. In non-dimensional form, with

$$\widehat{\sigma}_{ij} = \frac{2\sigma_{ij}rt}{F} \tag{5}$$

and with notations as used here, these solutions read

$$\widehat{\sigma}_{rr} = \frac{4r}{\pi}\Big[\frac{(r - \rho\cos\theta)(\rho - r\cos\theta)^2}{(r^2 + \rho^2 - 2r\rho\cos\theta)^2} + \frac{(r + \rho\cos\theta)(\rho + r\cos\theta)^2}{(r^2 + \rho^2 + 2r\rho\cos\theta)^2}\Big] - \frac{2}{\pi}\,, \tag{6}$$

$$\widehat{\sigma}_{\theta\theta} = \frac{4r}{\pi}\Big[\frac{(r - \rho\cos\theta)(r\sin\theta)^2}{(r^2 + \rho^2 - 2r\rho\cos\theta)^2} + \frac{(r + \rho\cos\theta)(r\sin\theta)^2}{(r^2 + \rho^2 + 2r\rho\cos\theta)^2}\Big] - \frac{2}{\pi}\,, \tag{7}$$

$$\widehat{\sigma}_{r\theta} = \frac{4r}{\pi}\Big[\frac{(r - \rho\cos\theta)(\rho - r\cos\theta)r\sin\theta}{(r^2 + \rho^2 - 2r\rho\cos\theta)^2} + \frac{(r + \rho\cos\theta)(\rho + r\cos\theta)r\sin\theta}{(r^2 + \rho^2 + 2r\rho\cos\theta)^2}\Big]\,. \tag{8}$$

Expressing the stress field in terms of $\sigma_{ij}(x, y)$, $i, j = x$ or y, as sketched in Figs. 3 to 5, enables a simpler interpretation with regard to the buckling of the disks under different loading and boundary conditions. These stress distributions could be obtained by rotational transformation of Eqs. (6) to (8), leading to quite lengthy expressions. Instead, for the sale of simplification, the shown stress distributions were computed by 2d finite element models for plane stress states.

In these figures, the isolines in the immediate near of the load application points – where, a stress singularity exists – were excluded for better presentation of the stress field, in the area, where they are relevant regarding buckling of the disks.

The stress levels related to the isolines refer to the non-dimensional stress quantities $\widehat{\sigma}_{ij}$ according to Eq. (5), by which the mean value of $\widehat{\sigma}_{xx}$ along the diameter in y-direction is 1.0. The coordinates in the diagrams in these figures are also normalized as $\widehat{x} = \frac{x}{r}$ and $\widehat{y} = \frac{y}{r}$, respectively.

Because of the linearity in the pre-buckling states, the stress distributions for CASEs A and C (disk under tensile loading) and those for B and D (disk under compressive loading), respectively, are related to each other simply via multiplication by −1. By this way, Figs. 3, 4, and 5 are representative for all CASEs.

For buckling under tension, the compressive stresses in y-direction in the mid-area of the disk—see Fig. 4, are the reason. The values of these compressive stresses are, however, considerably smaller than the compressive stresses in x-direction for CASEs B and D at the same load intensity, compare Fig. 3. Furthermore, the area, in which these compressive stresses in y-direction exist, is smaller than the area with compressive stresses in x-direction, which are relevant for buckling in CASEs B and D. Additionally, this area is surrounded by an area of tensile stresses in y-direction, which have a stabilizing effect. Thus, one should expect much higher critical load intensities for buckling under tension than for buckling under compression.

Remarks.

- (1) Because the conditions for the Michell theorem [32] are fulfilled, the stress distributions are independent of the Poisson's ratio of the material. This can also be seen in Eqs. (6)–(8).
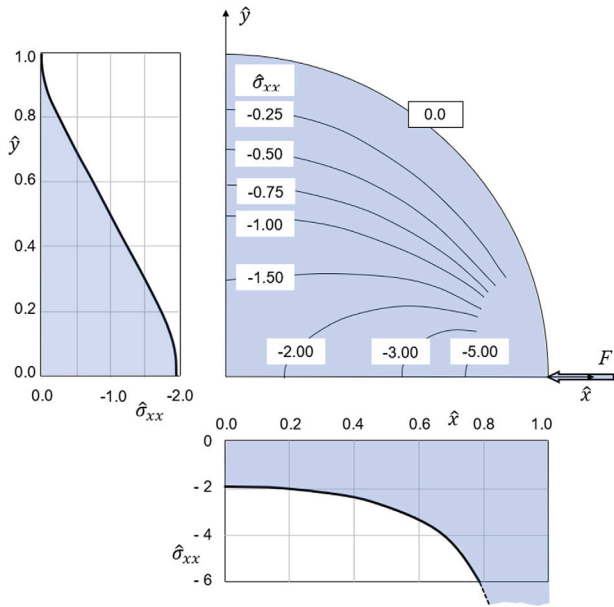
Fig. 3. Distribution of $\hat{\sigma}_{xx}$ for the disk under compressive loading (CASEs B and D).
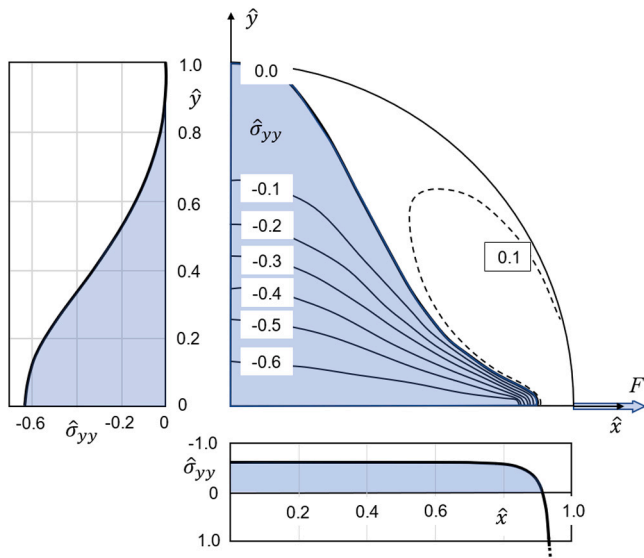

Fig. 4. Distribution of $\hat{\sigma}_{yy}$ for the disk under tensile loading (CASEs A and C).

Fig. 5. Distribution of $\hat{\sigma}_{xy}$ for the disk under tensile loading (CASEs A and C).

Fig. 6. Dependency of the critical load intensities on the thickness t and on the radius r, respectively, shown in double-logarithmic scales; upper diagram: $r = 200$ mm, $t \in [0.1, 0.5]$ mm; lower diagram $t = 0.5$ mm, $r \in [50, 350]$ mm; material with $E = 210\,000$ MPa, $\nu = 0.33$.

- (2) As a consequence of (1), it is clear that the following holds (chose, e.g., $\nu = 0.0$): In contrast to the situation of buckling of stretched strips clamped at the short edges, as discussed in [18, 20], the buckling relevant compressive stresses in y-direction of completely free or simply supported stretched disks are not caused by a restrained Poisson effect.

4.2. Critical load intensities

In parametric studies,in which the geometrical data were varied for all CASEs, A to D, critical load intensities were computed by solving the eigenvalue problems Eqs. (1) and (2), respectively. (By the way, both formulations of the eigenvalue problem have led to quite the same results.) The buckling behavior was investigated for the whole range of thermodynamically admissible values of the Poisson's ratio, i.e. for $\nu \in [-1, 0.5]$.
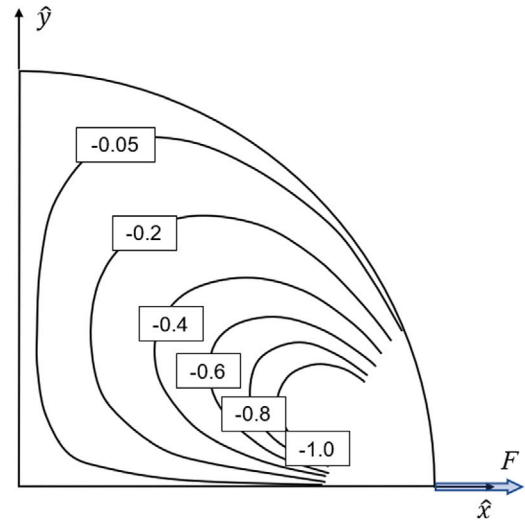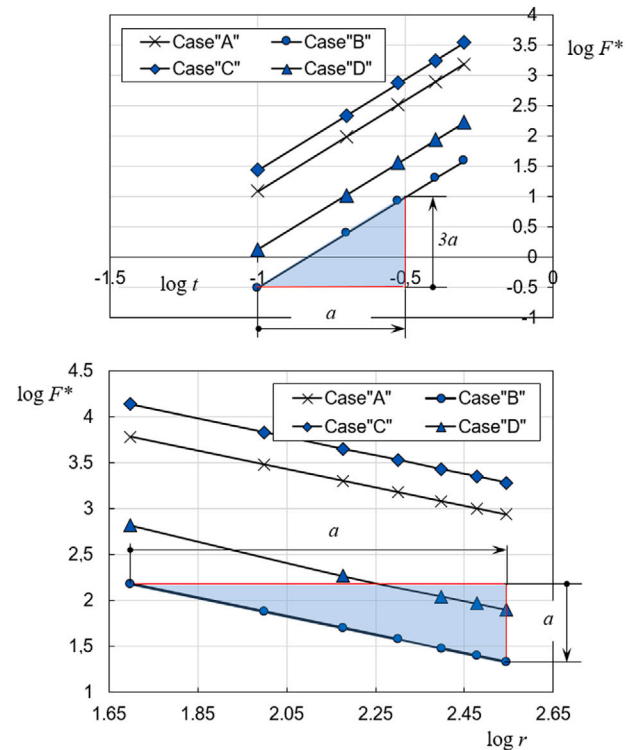
The upper diagram in Fig. 6, shows the critical load intensities when the radius of the disk is kept constant and the thickness is varied. The results represent straight lines with inclination 3.0 in double-logarithmic scales. This indicates an exponential dependence (exponent 3) of the critical load intensities on the thickness.

Variation of the radius of the disks when the thickness is kept constant leads to critical load intensities as shown in the lower diagram in Fig. 6. One can conclude that a hyperbolic relation exists between critical load and radius. The exponent is -1.
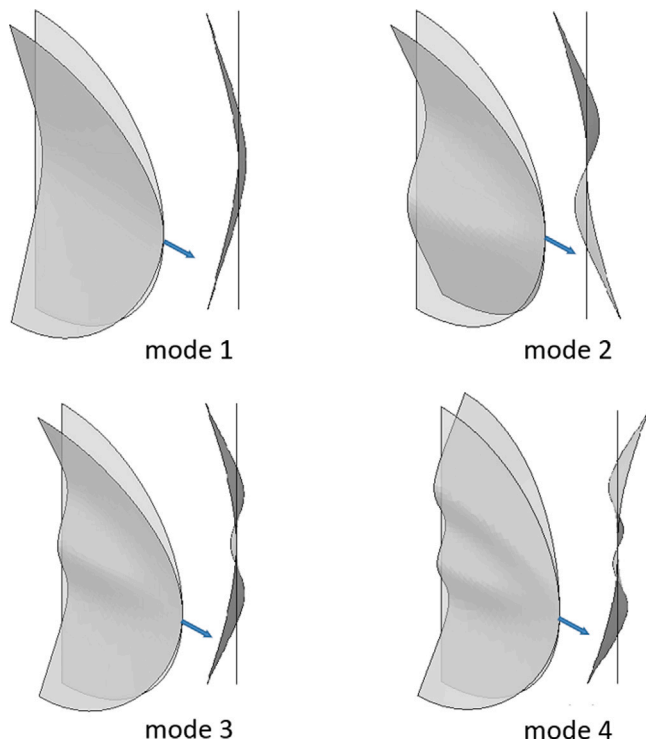
mode 1   mode 2

mode 3   mode 4

Fig. 7. Fundamental and higher order buckling modes of CASE A (free edge, tensile load).

CASE B   CASE C   CASE D

Fig. 8. Fundamental buckling modes for CASEs B, C, and D).

Fig. 9. Deviation of the buckling factors for different Poisson's ratios from that one for $\nu = 0.33$ in percent; the fine dotted line corresponds to Eq. (14).

4.3. Buckling factor "k"

In accordance with Buckingham's Pi-Theorem the following relation is obtained,

$$F^* \sim E \frac{t^3}{r} \, . \tag{9}$$

With the proportionality factor k_j, $j = $ A, B, C, or D, for each of the considered CASEs the above relation reads:

$$F_j^* = k_j E \frac{t^3}{r} \, . \tag{10}$$

The factor k_j is the so-called buckling factor, which has been determined from the results of the parametric study as

$$k_j = F_j^* \frac{r}{Et^3} \, . \tag{11}$$

in dependence of the Poisson's ratio ν.

4.4. Buckling modes

Using the eigenvectors ϕ_i obtained from solving the eigenvalue problems Eqs. (1) and (3), respectively, in conjunction with the shape functions of the elements, the buckling modes of order i were determined.

For CASE A, which is the most interesting case, the fundamental buckling mode as well as the next three higher modes are depicted in Fig. 7. Fig. 8 shows the fundamental buckling modes for the remaining CASEs B, C, and D. Presenting only half of the disk provides a clear characterization of the variations of the mode shapes. All shown modes are symmetrical with respect to the y-axis. One should notice that for CASE C, i.e., simply supported disk under tensile loading, the fundamental buckling mode (in the mid of Fig. 8) is, in contrast to the other cases, point-symmetrical.
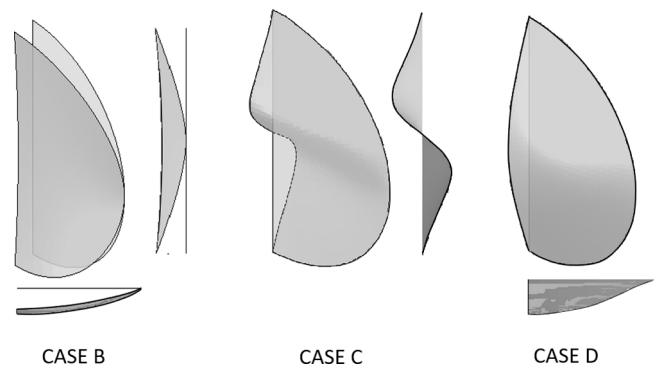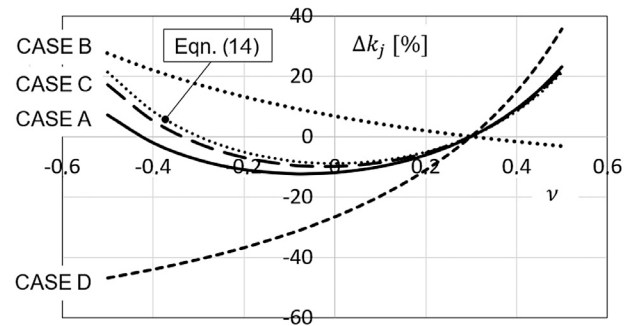
4.5. Influence of the values of Poisson's ratio—Considerations of auxetics

The static Föppl–v.Karman plate equation for pure in-plane loading reads

$$K\Delta\Delta w - (N_{xx} \frac{\partial^2 w}{\partial x^2} + N_{yy} \frac{\partial^2 w}{\partial y^2} + N_{xy} \frac{\partial^2 w}{\partial x \partial y}) = 0 \, , \tag{12}$$

with the Laplace operator Δ in Cartesian coordinates and $N_{ij} = t\,\sigma_{ij}$. K denotes the bending stiffness,

$$K = \frac{Et^3}{12(1-\nu^2)} \, . \tag{13}$$

With Eq. (12), in classical configurations of plate buckling, i.e., with homogeneous field of uni-axial stresses, the dependence of the buckling factors on the Poisson's ratio corresponds simply with the dependence of the plate's bending stiffness on ν, leading to

$$\frac{k(\nu_1)}{k(\nu_2)} = \frac{1-\nu_2^2}{1-\nu_1^2} \, , \tag{14}$$

for a given configuration, in which only the Poisson's ratio is varied. $k(\nu_j)$ is the buckling factor if in the considered configuration the material has a Poisson's ratio ν_j. With Eq. (14), for $\nu > 0$ the buckling factor would increase with increasing Poisson's ratio, and – because of ν appears as ν^2 in Eq. (14) – vice versa for $\nu < 0$.

However, our parametric studies with varied ν has led to different results. In Fig. 9, the deviation of the buckling factor due to a variation of ν in the interval $[-0.5, 0.5]$ from that one for $\nu = 0.33$ is shown in percent.

In the above Remark (1), it is stated, that ν has no influence on the stress field. Thus, the question arises, what are the reasons for a dependency of the buckling factors on the Poisson's ratio in addition to that what is caused by the dependency of the bending stiffness on ν?

Although the pre-buckling stress state is not affected by the value of the Poisson's ratio, the strains are dependent on ν, as it becomes
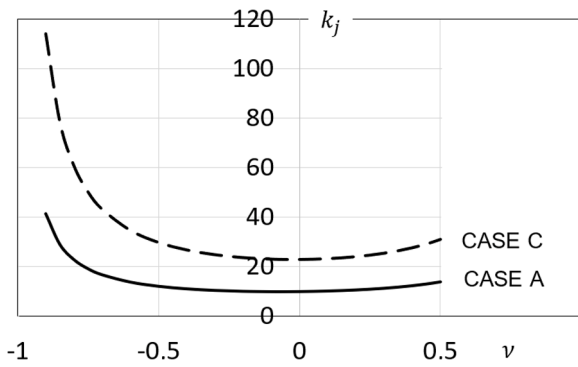
Fig. 10. Dependency of the buckling factor on the Poisson's ratio for CASEs A and C.
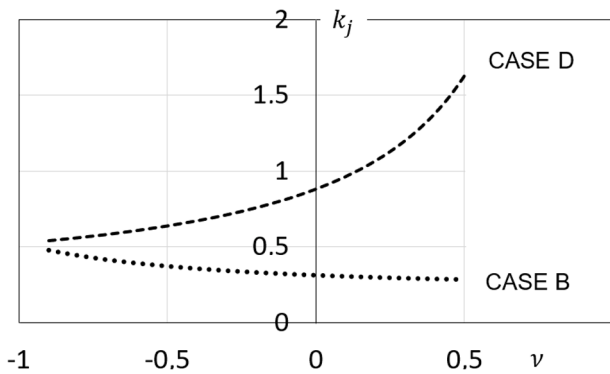

Fig. 11. Dependency of the buckling factor on the Poisson's ratio for CASEs B and D.

Fig. 12. Fundamental buckling mode for CASE B computed for different Poisson's ratios.

Table 2
Buckling factors; comparisons with values derived from published results; [7] and [8], respectively, refers to values derived from the cited literature, (∗) means that there are no values available from the literature.

ν	Buckling factor for			
	Free disks under		Simply supp. disks under	
	Tension CASE A	Compr. CASE B	Tension CASE C	Compr. CASE D
−1.0 - −0.1	(∗)	(∗)	(∗)	(∗)
0.0	(∗)	(∗)	22.78	0.882
			24.68 [8]	0.886 [8]
0.1	(∗)	(∗)	23.10	0.965
			23.27 [8]	0.968 [8]
0.2	(∗)	0.296	23.91	1.069
		0.298 [7]	23.27 [8]	1.071 [8]
0.3	(∗)	(∗)	25.31	1.202
			25.48 [8]	1.204 [8]
0.4	(∗)	(∗)	27.51	1.381
			27.68 [8]	1.381 [8]
0.5	(∗)	(∗)	30.91	1.632
			31.09 [8]	1.631 [8]

visible by the linear stress–strain relations for plane stress states, $\varepsilon_{xx} = \frac{1}{E}(\sigma_{xx} - \nu\sigma_{yy})$, $\varepsilon_{yy} = \frac{1}{E}(\sigma_{yy} - \nu\sigma_{xx})$, $\varepsilon_{xy} = \frac{1}{2G}\sigma_{xy}$.

Since $G = \frac{E}{2(1+\nu)}$, the Poisson's ratio influences the shear strains resulting from shear stresses in a noticeable way. (Consider, e.g., the situation when $\nu \to -1$.)

In consequence of this influence of ν on the strains, also the distribution of the strain energy density, $\frac{1}{2}\sigma_{ij}\varepsilon_{ij}$, depends on ν. This is, why – despite the stress fields are not influenced by ν – the buckling factors show a dependence on the Poisson's ratio.

Fig. 9 shows that for CASEs A and C the influence of ν is very close to that indicated by Eq. (14). This is, because the higher values of the buckling relevant compressive stresses σ_{yy} are quite homogeneously distributed over an area along the x-axis and the shear stresses are very small there, compare Figs. 4 and 5. Thus, this kind of buckling is – in some sense – comparable with buckling of a plate with large length to width ratio loaded transversely to its long axis, for which the buckling mode is independent of ν and for which Eq. (14) is applicable. However, with larger absolute values of negative Poisson's ratios, the inhomogeneity of the stress field and, particularly the influence of shear come more into play, resulting in a rapid increase of the k-values.

Fig. 10 shows the dependency of the buckling factors on the Poisson's ratio for CASEs A and C far into the range of auxetic materials, and Fig. 11 shows this dependency for CASEs B and D.

Already from Fig. 9 one sees that for CASEs B and D the dependence of the buckling factors on ν deviates significantly from that what Eq. (13) would predict. This is caused by the strongly inhomogeneous distribution of the buckling relevant compressive stresses σ_{xx}, see Fig. 3. The fundamental buckling modes are no longer that much localized to the area along the x-axis but include also areas with large shear stresses, see Fig. 5. Thus, the buckling modes are influenced by ν. For instance, in Fig. 12 the fundamental buckling mode for CASE B is shown for $\nu = -0.85$, $\nu = 0.0$, and $\nu = 0.4$. The surface of the buckled disk varies from double curved with negative Gaussian
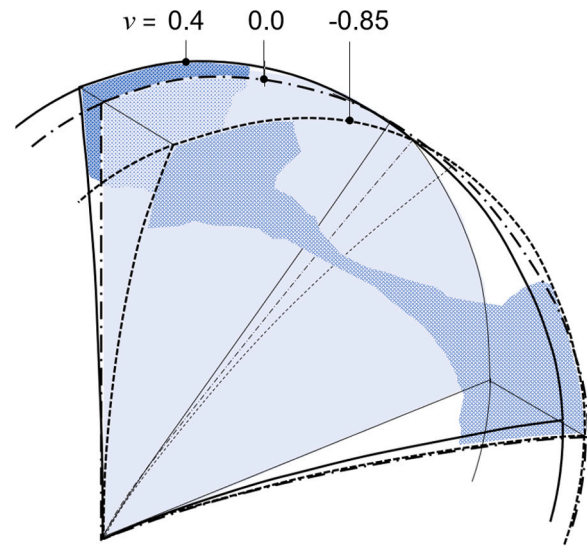
curvature to single curved and again to double curved, however with positive Gaussian curvature. Such essential changes in the buckling mode, and thus, resulting changes in the distribution of the curvature, in combination with a fixed but inhomogeneous distribution of the pre-buckling stresses and with strain fields, which depend on ν, lead to quite different strain energies and, consequently, to substantial changes in the critical load intensities. This is an effect, which comes in addition to the influence of ν caused by the variation of the bending stiffness according to Eq. (13).

Having all these effects in mind, it is clear that one hardly can forecast the influence of the Poisson's ratio without performing parametric studies. The described tendencies for $k(\nu)$ are confirmed by k-values derived from former papers, where such values are available, see comparisons in Table 2.

5. An additional consideration, CASE E

Comparing the fundamental buckling mode of the completely free disk under tension loading with the photograph shown in Fig. 1(d), i.e., stretched pourer disk, one does not see too much correspondence. In order to show that this discrepancy comes from the different kind of load application, we analyzed the stretched disk as sketched in Fig. 13.
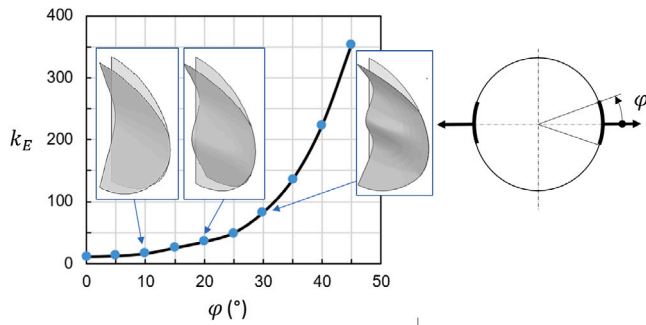
Fig. 13. Buckling factor and buckling modes for CASE E in dependence of φ; $v = 0.33$.

Fig. 14. (a) Load vs. displacement diagram showing the character of the post-buckling behavior for CASE A with $v = 0.33$ (black line) and $v = -0.5$ (gray line); (b) Detail of (a) showing the region of the secondary bifurcation; (c) deformed disk from view point along x-axis before (marked by an asterisk) and after the secondary bifurcation (marked by a ring), respectively. A disk with $r = 200$ mm, $t = 0.5$ mm, $E = 210\,000$ MPa was examined.

There, the portion of the edge of the disk in the interval $[-\varphi, +\varphi]$ was assumed to be a rigid boundary, movable only in the x-direction. By this way, the force F is introduced to the disk rather as a distributed load than a as a point load. Furthermore, these boundary conditions might come close to the clamping effect which the pourer disk experiences between thumb and index finger.

In Fig. 13, the buckling factor and the fundamental buckling mode are shown in dependence of the angle φ. The buckling mode computed for $\varphi = 30^\circ$ has a certain resemblance to the post-buckling pattern as shown in Fig. 1(d). Considering the buckling factor for this value of φ, one realizes that the difference between the load intensities required for making the pourer disk buckle under compression and under tension, respectively, is even larger than for that between CASEs A and B, which is already substantial. Thus, convince yourself, whether or not you have sufficient power for bringing a pourer disk to buckling under tension before you demonstrate this phenomenon to others!

6. The post-buckling behavior

The post-buckling behavior was analyzed for the completely free stretched and compressed disk, respectively, i.e., for CASEs A and B.

In Figs. 14, 15, and 16, the out-of-plane displacements of specified points, all normalized by the thickness of the disk, i.e. $\hat{w} = w/t$, are shown in dependence of the load intensity $\hat{F} = F/(2rt)$.

For CASE A in Fig. 14, the force vs. the out-of-plane displacement $\hat{w}$ of the upper vertex is shown, and Fig. 15 presents the post-buckling behavior for six indicated points around the circumference of the disk. Fig. 16 shows the post-buckling behavior for CASE B. There, $\hat{w}$ represents the force vs. out-of-plane displacement of the mid-point of the disk.

In CASE A (Fig. 14), it is shown that after the initial bifurcation the post-buckling behavior is stable at first. However, the deformation pattern switches at relatively low tensile forces. For the case of $v = 0.33$, at $\hat{w} \approx 10$ the initially rather steep ascent in the function graph decreases and the V-shaped deformation gets some waviness; see the boxes (c) in Fig. 14, which represent the deformed disk from the point of view along the x-axis just before and after the post-buckling bifurcation. Furthermore, from Fig. 15 one can conclude that after the initial bifurcation the disk does not fold up exactly symmetrically but the upper vertex displaces more than the lower vertex. This is not caused by a slight global rotation around the x-axis but represents the contribution to the deformation pattern, which corresponds to the higher-order point-symmetrical buckling modes; compare Fig. 7. Most interesting is the observation that the secondary bifurcation is accompanied by a short combined twisting and wiggling around the diameter normal to the loading direction; see detail in Fig. 15.

Fig. 16 exhibits the process of deforming the disk under compressive forces (CASE B) towards a circular cylinder by simply increasing the loading. This figure reminds to that what was mentioned with respect to the bottle pourer in the Introduction. Furthermore, it shows that there
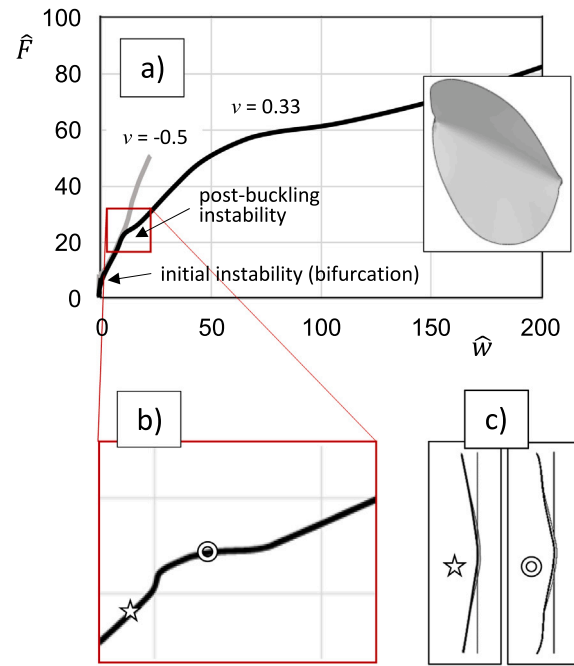
exists a maximum out of plane deformation $\hat{w}$, from which on further increase of the compression leads to a decrease of $\hat{w}$. This is quite similar to that what can be observed for the elastica, simply supported at both ends, when its ends meet each other and continue moving along its original axis, see e.g. [33].

7. Conclusions

Buckling and post-buckling analyses are presented for thin circular disks made of homogeneous, linear elastic material under compressive and tensile loading along a diameter. In addition to comparisons with earlier published results, in this paper the not yet examined but quite interesting case of the completely free stretched disk is treated. The investigations into the stability behavior of disks made of auxetic material are of particular novelty. Furthermore, interesting effects appearing in the post-buckling range are presented and discussed.

7.1. Buckling factors

Similar to classical plate buckling and in accordance with Buckingham's *Pi*-Theorem, the critical load can be expressed by $F_j^* = k_j E \frac{t^3}{r}$, with k being the so-called buckling factor. k depends on v only, i.e., it is independent of the disk's radius and thickness as well as on the Young's modulus of its material. This buckling factor has been determined for disks under different loading and boundary conditions (denoted as CASEs A to E in the following) in dependence of the Poisson's ratio v of the material in the thermodynamically admissible range, i.e. $v \in [-1, 0.5]$. Some quite peculiar results are presented. For instance, despite the fact that the stress state is independent of v, the buckling factors exhibit a dependence on v, which for some cases differs significantly from that what one might expect if one only considers the dependence of the bending stiffness on the Poisson's ratio.

CASE A: completely free disk under tensile loading. This is the most interesting configuration. It has not been investigated in previous
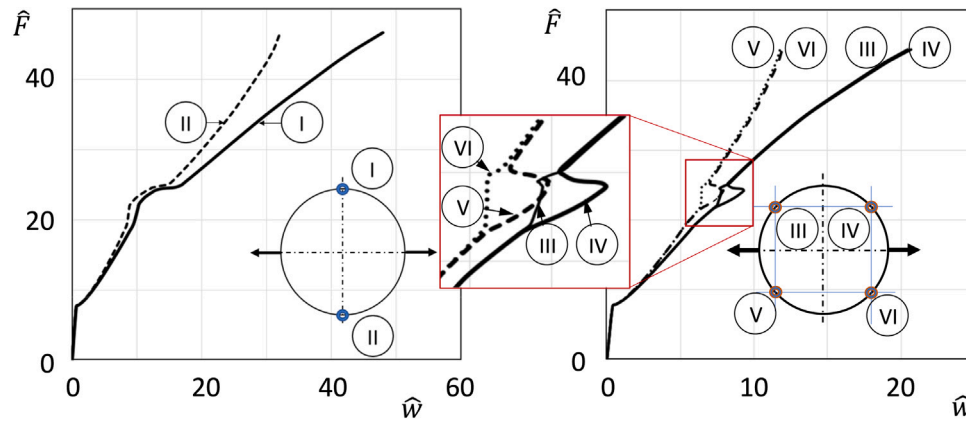
Fig. 15. CASE A: Load vs. out-of-plane displacement diagram of six points along the circumference of the disk. The detail shows a combined twisting and wiggling in the region of the secondary bifurcation.
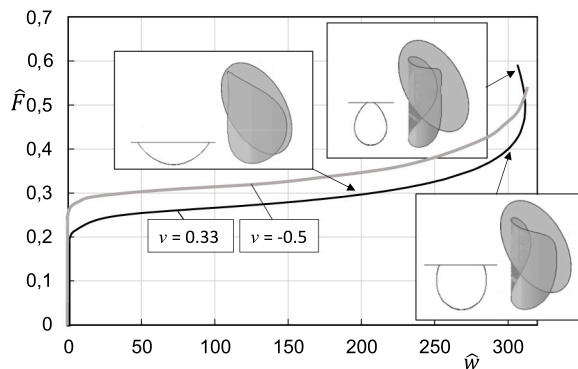

Fig. 16. Load vs. displacement diagram showing the character of the post-buckling behavior for CASE B for $v = 0.33$ (black line) and $v = -0.5$ (gray line). A disk with $r = 200$ mm, $t = 0.5$ mm, $E = 210\,000$ MPa was examined.

papers. The buckling factors for this case are much larger than for compressive loading, i.e., CASE B. For instance, for $v = 0.3$ there is a factor of about 30 between them. The dependence of k on the Poisson's ratio corresponds nearly to that of the bending stiffness. This holds initially also for investigations of disks made of auxetic material. However, in the range $v \to -1$, the buckling factor increases sharply.

CASE B: completely free disk under compressive loading. This configuration has been considered earlier in [7], without considering post-buckling. In [7] a semi-analytical procedure (a Ritz-method) was applied and the critical load has been computed for a Poisson's ratio $v = 0.2$. After expressing this result by a buckling factor as defined in the present paper (by Eq. (11)), a good agreement with our result for this value of v was found. For this configuration, the new results provide the dependence of k on v within the whole thermodynamically admissible range and exhibit a completely unexpected behavior: In contrast to the other considered configurations, in CASE B the buckling factor increases monotonically with decreasing values of v.

CASE C: disk simply supported along the whole boundary, loaded by tensile forces. This configuration is mentioned in [6] and considered in [8] for discrete values of $v \in [0.0, 0.5]$. The buckling factors presented here compare quite well with the values presented in [8]. Similar to CASE A, the extension of the investigations to disks made of auxetic material initially shows a dependence of k on v corresponding nearly to that of the bending stiffness. As in CASE A, in the range $v \to -1$ the buckling factor increases sharply.

CASE D: equivalent to CASE C; however, loaded by compressive forces. This configuration represents a special case in [8] and the buckling factors compare well with the here presented results. In the

present paper, where the range of negative Poisson's ratios is treated, too, also for this configuration an unexpected dependence of k on v was found: The buckling factor decreases monotonically with decreasing values of v even in the range of negative values of v. This is in contradiction to that what should happen when just the influence of v on the bending stiffness would be taken into account.

CASE E: equivalent to CASE A; however, the tensile load is distributed along sections of the boundary. For this configuration the buckling factor has been determined in dependence of the angle of the loaded portion of the edge of the disk. Keeping the resultant of the distributed tensile load as relevant force, the buckling factor increases strongly with increased angle of the load application area.

7.2. The post-buckling behavior

The post-buckling behavior is presented for disks under conditions corresponding to the above described configurations CASE A and CASE B, i.e. for completely free disks. After buckling has appeared, such disks deform under tension (CASE A) by developing a rather strongly curved fold along the loaded diameter. A monotonic increase of the out-of-plane displacement of the circle vertexes at the diameter normal to the loading direction is observed, while the diameter, along which the loading acts, remains nearly undeformed. Initially, the projection of the deformed disk in the direction of the loaded diameter looks like a wide opened letter V. Then, caused by a secondary bifurcation a mode change happens and the flanks of the V get some waviness. At this secondary bifurcation a slight combined twisting and wiggling of the disk around the diameter normal to the loading direction takes place.

In contrast, the free disk under compressive loads (CASE B) behaves quite unspectacularly in the post-buckling regime. The diameter, along which the loading acts, is bent, and the diameter normal to the loading direction is moved nearly without any deformation, so that the disk can easily be curled to form a cylinder (as it is the case when it is, e.g., used as a bottle pourer).

7.3. General remarks

The considerations and the achieved results are interesting for scientists working in the field of stability and for engineers in lightweight design of structures. There are a number of applications of the here presented findings in mechanical engineering, in process plants, in

medical technology and sensorics as well as for describing the behavior of devices in flexible electronics and of biological membranes.

CRediT authorship contribution statement

Saeideh Faghfouri: Data collection, Data analysis and interpretation, Final approval of the version to be published. **Franz G. Rammerstorfer:** Conception or design of the work, Data analysis and interpretation, Drafting the article, Critical revision of the article, Final approval of the version to be published.

Declaration of competing interest

The authors declare that they have no known competing financial interests or personal relationships that could have appeared to influence the work reported in this paper.

Acknowledgment

References

[1] Timoshenko StP, Gere JM. Theory of elastic stability. New York and London: McGraw-Hill; 1961.

[2] Brush DO, Almroth BO. Buckling of bars, plates and shells. New York: McGraw-Hill; 1975.

[3] Parkus H. Mechanik Der Festen KÖrper. Wien: Springer-Verlag; 1966.

[4] Rammerstorfer FG. Increase of the first natural frequency and buckling load of plates by optimal fields of initial stresses. Acta Mech 1977;27:217–23.

[5] Cuong-Le Thanh, Nguyen Khuong D, Nguyen-Trong N, Khatir Samir, Nguyen-Xuan H, Abdel-Wahab M. A three-dimensional solution for free vibration and buckling of annular plate, conical, cylinder and cylindrical shell of FG porous-cellular materials using IGA. Compos Struct 2021;259:113216.

[6] Durban D. Instability of an elastic circular plate subjected to nonuniform loads. AIAA J 1977;15:360–5.

[7] Rozsa M. Stability analysis of a circular plate submitted to two compressive forces acting along a diameter. Diameter, Acta Techn Acad Scientiarum Hungaricae 1966;55:153–72.

[8] Ayoub EF, Leissa AW. Free vibration and tension buckling of circular plates with diametral point forces. J Appl Mech 1990;57:995–9.

[9] Leissa AW, Ayoub EF. Tension buckling of rectangular sheets due to concentrated forces. J Eng Mech 1989;115:2749–62.

[10] Friedl N, Rammerstorfer FG, Fischer FD. Buckling of stretched strips. Comput Struct 2000;78:185–90.

[11] Cerda E, Ravi-Chandar K, Mahadevan L. Thin films: wrinkling of an elastic sheet under tension. Nature 2002;419:579–80.

[12] Silvestre N. Wrinkling of stretched thin sheets: Is restrained Poisson's effect the sole cause? Eng Struct 2016;106:195–208.

[13] Jacques N, Potier-Ferry M. On mode localisation in tensile plate buckling. C R Mec 2005;333:804–9.

[14] Jacquesa N, Elias A, Potier-Ferry M, Zahrouni H. Buckling and wrinkling during strip conveying in processing lines. J Mater Process Techn 2007;190:33–40.

[15] Puntel E, Deseri L, Fried E. Wrinkling of a stretched thin sheet. J Elast 2011;105:137–70.

[16] Kim Tae-Yeon, Puntel E, Fried E. Numerical study of the wrinkling of a stretched thin sheet. Int J Solids Struct 2012;49:771–82.

[17] Toth F, Rammerstorfer FG, Cordill MJ, Fischer FD. Detailed modelling of delamination buckling of thin films under global tension. Acta Mater 2013;61:2425–33.

[18] Rammerstorfer FG. Buckling of elastic structures under tensile loads. Acta Mech 2018;229:881–900.

[19] Huang Q, Yang J, Huang W, Giunta G, Belouettar S, Hu H. The boundary effects on stretch-induced membrane wrinkling. Thin-Walled Struct 2020;154:106838.

[20] Faghfouri S, Rammerstorfer FG. Mode transitions in buckling and post-buckling of stretched-twisted strips. Internat J Non-Linear Mech 2020;127:103609, 1-10.

[21] Zaccaria D, Bigoni D, Noselli G, Misseroni D. Structures buckling under tensile dead load. Proc R Soc Lond Ser A Math Phys Eng Sci 2011;467:1686–700.

[22] Bigoni D, Misseroni D, Noselli G, Zaccaria D. Effects of the constraint's curvature on structural instability: tensile buckling and multiple bifurcations. Proc R Soc Lond Ser A Math Phys Eng Sci 2012;468:2191–209.

[23] Lakes RS. Design considerations for materials with negative Poisson's ratios. J Mech Des 1993;115:696–700.

[24] Obrecht H, Reinicke U, Walkowiak M. Auxetische Strukturen - Neue Wege zu gewichtseffizienten Konstruktionen. Lightweight Design 2011;5:37–42.

[25] Rushchitsky JJ. To modeling the auxetic materials: some fundamental aspects. Math Model Comput 2014;1:97–108.

[26] Ghavidelnia N, Bodaghi M, Hedayati R. Idealized 3D auxetic mechanical metamaterial: an analytical, numerical, and experimental study. Materials 2021;14:993. http://dx.doi.org/10.3390/ma14040993.

[27] Hößl B, Böhm HJ, Rammerstorfer FG, Barth FG. Mechanoreception in the exoskeleton of arachnids: engineering meets biology. Calgary, Alberta: actapress.com; 2005.

[28] Hößl B, Böhm HJ, Schaber CF, Rammerstorfer FG, Barth FG. Finite element modeling of arachnid slit sensilla: II. Actual lyriform organs and the face deformations of the individual slits. Comp Physiol A 2009;195:881–94.

[29] Böhm HJ. CARINA - computer aided research in nonlinear analysis, program revisons 2.1.3 and higher. Vienna: Institute of Lightweight Design and Structural Biomechanics, Vienna University of Technology; 2013.

[30] Abaqus analysis user's guide version 6.20. 2020, https://abaqus-docs.mit.edu/%7E{}uno/abcde.html.

[31] Paige CC. Accuracy and effectiveness of the lanczos algorithm for the symmetric eigenproblem. Linear Algebra Appl 1980;34:235–58.

[32] Michell JH. On the direct determination of stress in an elastic solid, with application to the theory of plates. Proc London Math Soc 1899;31:100–24.

[33] Levien R. The elastica: A mathematical history. Technical Report No. UCB/EECS-2008-103, University of California at Berkeley; 2008.